CCUS: 4003166

A Deep Learning-Based Surrogate Model for Rapid Assessment of Geomechanical Risks in Geologic CO2 Storage

Fangning Zheng*[1], Birendra Jha[1], Behnam Jafarpour[1], 1. University of Southern California.

Abstract

Simulating CO_2 storage under geomechanical risks frequently involves substantial computational costs due to the coupling between multiphase flow and geomechanics. Implementing standard workflows, such as well location optimization, with such coupled physics models can significantly increase the computational overhead and make the models impractical to use. We study the feasibility of using deep-learning models to significantly reduce the computational overhead associated with simulating and quantifying the geomechanical risks of CO_2 storage. The proposed approach leverages deep learning-based surrogate modeling to significantly enhance the efficiency of coupled flow-geomechanics simulations for identifying suitable injection well locations for CO_2 storage. Using simulated data, we train a U-Net convolutional neural network to learn a mapping between well locations s and spatially distributed model parameters (permeability) to the simulation outputs of interest. Once trained with a fixed set of model input parameters, the U-Net model can map different well location scenarios to the corresponding pressure fields, CO_2 saturation, and geomechanical outputs, including vertical displacement and plastic strain. The U-Net model is subsequently adopted as an efficient tool to replace the coupled flow-geomechanics simulation needed for identification of injection well locations to minimize geomechanical risks. We report preliminary results showing that the trained U-Net model can predict pressure and saturation fields from well locations, with all the other inputs remaining consistent with the simulation model used in the training. We investigate the performance of the network under different assumptions and for estimating different flow and geomechanical outputs. The results show that the U-Net model can drastically reduce the computational cost of well placement workflows by replacing coupled physics simulation with a fast proxy model that can be used to predict the geomechanical risk associated with different well location and injection strategies. The developed framework can be used to improve the computational demand of coupled-physics modeling and facilitate its application to decision-making workflows and field management.

Introduction

Carbon Capture and Storage (CCS) has gained recognition as a prominent option for mitigating industrial CO_2 emissions and has earned considerable attention in recent literature. This attention encompasses various aspects, including CO_2 capture and storage mechanisms (Chow et al., 2003; Rosenbauer and Thomas, 2010; Blunt, 2010; Kumar et al., 2005; MacMinn et al., 2010; Nordbotten et al., 2004), analytical and numerical solutions (Nordbotten et al., 2005; Dentz and Tartakovsky, 2009; Mathias et al., 2009b; Pruess and Garcia, 2002; Nghiem et al., 2004; Mukhopadhyay et al., 2015), simulations integrating CO_2 storage with coupled flow-geomechanics (Dean et al., 2006; Longuemare et al., 2002; Vilarrasa et al., 2011; Rutqvist et al., 2010; Goodarzi et al., 2010; Verdon et al., 2011; Jha and Juanes, 2014; McMillan et al., 2019; Zhao and Jha, 2019), field-scale optimization focusing on maximizing CO_2 storage through solubility trapping and capillary trapping mechanisms under well-controlled or well-placement optimization (Zheng et. al., 2021; Shamshiri and Jafarpour, 2011; Zhang and Agarwal, 2012; Heath et al., 2014; Goodarzi et al., 2015), and risk assessment problems primarily focuses on mitigating geomechanical risks such as injection/production-induced ground displacement, induced micro-seismicity, and CO_2 leakage potential through caprock, wellbore, and other pathways (Brandt et al., 2014; Birkholzer et al., 2015; Wilson et al., 2003; Celia et al., 2015; Zoback and Gorelick, 2012; Zheng et al., 2023).

Simulating CO_2 storage under geomechanical risks frequently involves substantial computational costs attributed to the coupling between flow and geomechanical models. When history matching, optimization, and (geological) uncertainties are introduced, the computational burden can increase significantly, thereby limiting the industrial-scale applications of these workflows. There are mainly four surrogate modeling approaches (Bahrami et. al., 2022; Jaber et. al., 2019; Syed et. al., 2022) for alleviating computational costs in the application of reservoir simulation: 1) Statistical approaches rely on statistical methods to construct a response surface, effectively simplifying the problem. They aim to alleviate both complexity and computational burden, making it possible to predict reservoir performance under geological uncertainties more efficiently (Chu, 1990; Elvind et al., 1992; Dejean and Blanc, 1999; Friedmann et al., 2003; Manceau et al., 2001; Eide et al., 1994; White and Royer, 2003; Kabir et al., 2004; Yeten et al., 2005; Kalla and White, 2007; Li and Friedmann, 2005; Slotte and Smorgrav, 2008; Schuetter et al., 2014). Statistical approaches are reliable if the estimated values closely align with the actual values within an acceptable margin of error (Jaber et. al., 2019). 2) Reduced-physics methods simplify the physical models using different techniques, such as multi-fidelity grid resolution, to expedite computations (Al-Mudhafar et al., 2022; Ganesh and Mishra, 2014; Gasda et al., 2012; Saripalli and McGrail, 2002; Benson, 2003; Noh et al., 2007; Burton et al., 2008; Oruganti and Mishra, 2013). 3) Reduced order modeling (ROM) involves projecting the high-dimensional system matrix onto a lower-dimensional space, enabling faster solving of equations while excluding irrelevant parameters (Jin and Durlofsky, 2018; Harp et al., 2016; Jia et al., 2016; He and Durlofsky, 2014; Chen et al., 2018; Keating et al., 2016; Gilmore et al., 2022; Cardoso et al., 2009; Van Doren et al., 2006; Ghasemi et al., 2015; Slotte and Smorgrav, 2008). 4) AI-based models are surrogate models that are trained using machine learning and pattern recognition techniques to create an input-output mapping. The field of AI-based models can be broadly categorized into two major groups: data-driven proxy models that are trained purely based on data acquired from physics-based simulation modeling or monitoring/historical field data (Alenezi and Mohaghegh, 2016; Agada et al., 2017; Landa and Güyagüler, 2003; Qin et al., 2023), and physics-informed or physics-based proxy models that, in addition to using data, incorporate some aspects of the underlying physics into the model, e.g., by updating the loss function and structure of the machine learning model (Shokouhi et al., 2021; Liu et al., 2023; Meguerdijian et al., 2023; Jiang et al., 2023; Yan et al., 2022; Latrach et al., 2023).

Numerous studies have delved into the development of surrogate models for CO_2 storage, primarily with the objective of predicting trapping mechanisms and storage outcomes (Khanal and Shahriar, 2022).

State-of-the-art neural network architectures, including convolutional neural networks, U-Net, recurrent neural networks, LSTM, Residual neural networks, among others, have been harnessed to forecast the spatial and temporal evolution of pressure and CO_2 plume behavior in 2-D or 3-D fields characterized by heterogeneous flow properties and fixed well locations (Wen et al., 2022; Zhong et al., 2019). Understanding the geomechanical responses resulting from CO_2 injection is pivotal for ensuring the safety and effectiveness of injection operations within the designated storage timeframe. Notably, researchers have made strides in developing CO_2 storage surrogate models capable of predicting the spatial and temporal evolution of elastic geomechanical responses, such as stress and strain fields (Syed et al., 2022; Tang et al., 2022). Furthermore, a substantial body of research has been dedicated to the development of surrogate models aimed at facilitating the optimization of CO_2 storage, whether online or offline (Al-Mudhafar and Rao, 2017; Pan et al., 2014; Sayyafzadeh, 2017).

However, predicting the response of the field under varying well locations remains challenging due to the significant spatial variability of pressure and other state variables in response to changing well locations within heterogeneous flow property fields. Moreover, predicting the inelastic behavior of geomechanical responses, such as plastic strain, is an intricate task due to the spatial and temporal non-linearities involved (Zheng et al., 2021; Zheng et al., 2023). A critical gap in the existing literature is the development of surrogate models capable of predicting the spatial characteristics of state variables, including non-linear geomechanical responses such as plastic deformation, while accommodating well location changes. In this work, we build an efficient CO_2 storage surrogate model designed to facilitate the transformation of well location data and permeability field information into key state variables of interest. These state variables encompass 3-D pressure, CO_2 plume, ground displacement, and plastic deformation of the storage field. Our constructed surrogate models offer substantial versatility and can be effectively employed in various applications, including data assimilation, field-scale optimization, and history matching. Their primary benefit lies in their ability to significantly cut down on computational costs while enabling the practical implementation of decision-making workflows that closely align with real-world scenarios.

Methodology

The governing equations for the coupled flow-geomechanics model have been comprehensively explained in our prior publication (Zheng et al., 2021). Furthermore, the numerical simulation model used in generating the training samples in this paper is extensively documented in the Numerical Experiment Results Section, Example 2: Multi-facies Model in that prior work, including model configurations and simulation details. To conserve space and ensure a seamless flow of new content in this paper, we omitted the details of the governing equations and the numerical simulation model.

U-Net Surrogate Model

In this section, we present the architecture of the U-Net surrogate model that has been developed for the purpose of mapping 3-D input data fields encompassing well locations and permeability fields to 3-D output data, which includes pressure, vertical displacement, and CO_2 plume fields, at the last time step of simulation. Additionally, we outline the schematic workflow employed to map from well locations as input data to the ultimate generation of a 3-D plastic strain field as the desired output data, involving an intermediate step in the process. Figure 1 illustrates the U-Net architecture we have created. The model's input data dimension is configured as 56×56×20 in the x-, y-, and z-directions, and the output data dimension mirrors this setup. In the input dataset, we combine the well location data with the deterministic permeability field, represented in the fourth dimension. To encode the well location dataset, we utilize one-hot encoding, where cells are marked "1" at the perforation locations within a 3-D grid,

while the remaining cells are designated as “0”. We apply min-max normalization to standardize the input and output dataset.

The network is designed with a U-shaped architecture, comprising a contracting path and an expansive path. The contracting path is a standard convolutional network, featuring a series of convolution operations followed by a Leaky Rectified Linear Unit (Leaky-ReLU). Notably, a single down-sampling operation occurs at the third convolution layer within the contracting path to reduce dimensionality. During the contraction phase, spatial information is reduced while feature information is amplified. Conversely, the expansive pathway integrates both feature and spatial information by employing deconvolutions and concatenating high-resolution features from the contracting path. In this case, a single deconvolutional operation is carried out, with Leaky-ReLU serving as the activation function. In our design, we opt for a single down-sampling and up-sampling operations on the input data. This choice is deliberate, aimed at retaining a significant portion of the spatial information while maintaining a manageable number of model parameters. This balance between preserving spatial information and managing model parameters ensures a trade-off between model accuracy and training efficiency. To enhance network depth while maintaining efficiency, we incorporate four residual blocks into the U-Net structure. These residual blocks, with skip connections, contribute to creating a deeper convolutional neural network. This approach has been shown to yield improved performance (Chen et al., 2022; Jiang et al., 2021). Figure 2 provides an in-depth view of the model structure. The U-Net model we have crafted comprises three primary layer types: convolutional layers, residual layers, and deconvolutional layers. Figure 2 encapsulates the layer types, their corresponding output shapes, and the parameter count for each layer. The complete model comprises approximately 1.5 million parameters. We apply Leaky Rectified Linear Unit (Leaky ReLU) as the activation function after each convolutional layers to avoid the dying ReLU problem (Nair and Hinton, 2010). The Gaussian Error Linear Units (GELUs) activation function is applied in the last layer to prevent negative output values (Hendrycks and Gimpel, 2016).

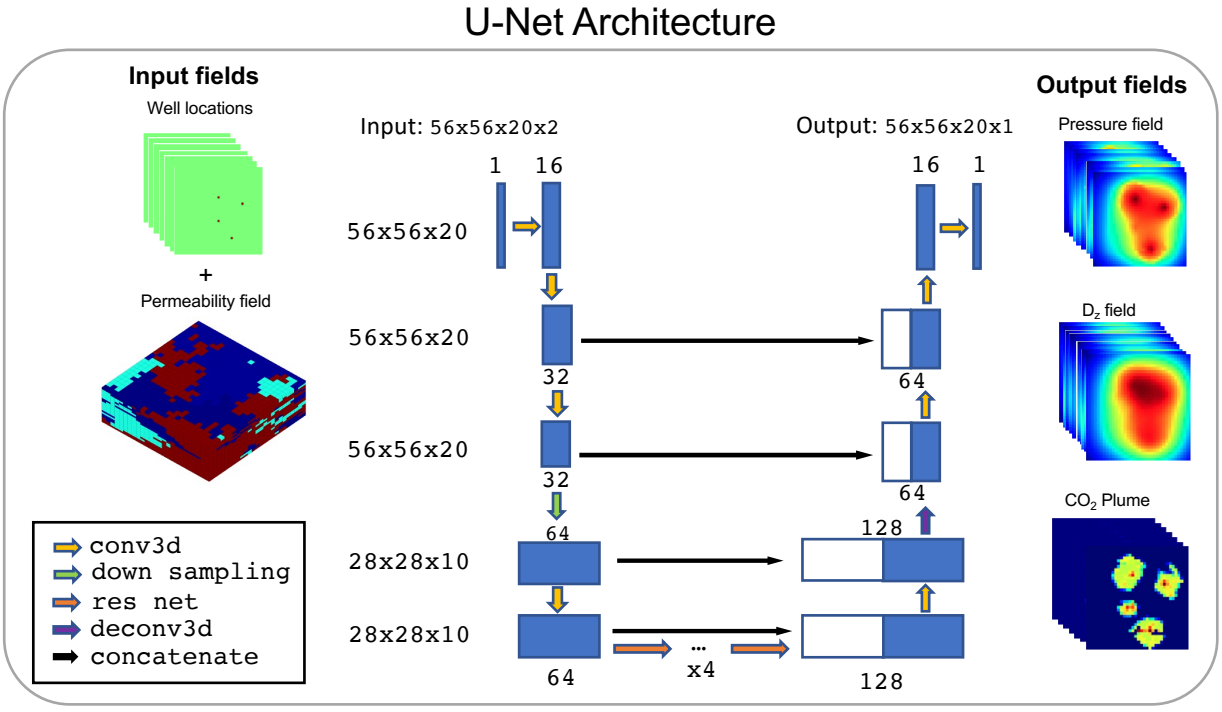

Figure 1. U-Net architecture for mapping from 3-D input data including well locations and permeability fields to 3-D output data including pressure, vertical displacement, and CO_2 Plume fields.

Convolutional Layers

Block type	Layer type	Output shape	# of parameters
	Conv3d	(16, 56, 56, 20)	880
Convolution block	Conv3d	(32, 56, 56, 20)	13,856
	GroupNorm	(32, 56, 56, 20)	64
	LeakyReLU	(32, 56, 56, 20)	0
Convolution block	Conv3d	(32, 56, 56, 20)	27,680
	GroupNorm	(32, 56, 56, 20)	64
	LeakyReLU	(32, 56, 56, 20)	0
Convolution block	Conv3d	(64, 28, 28, 10)	55,360
	GroupNorm	(64, 28, 28, 10)	128
	LeakyReLU	(64, 28, 28, 10)	0
Convolution block	Conv3d	(64, 28, 28, 10)	110,656
	GroupNorm	(64, 28, 28, 10)	128
	LeakyReLU	(64, 28, 28, 10)	0

Residual Layers

Block type	Layer type	Output shape	# of parameters
Residual block	Conv3d	(64, 28, 28, 10)	110,656
	GroupNorm	(64, 28, 28, 10)	128
	LeakyReLU	(64, 28, 28, 10)	0
	Conv3d	(64, 28, 28, 10)	110,656
	GroupNorm	(64, 28, 28, 10)	128
Residual block	Conv3d	(64, 28, 28, 10)	110,656
	GroupNorm	(64, 28, 28, 10)	128
	LeakyReLU	(64, 28, 28, 10)	0
	Conv3d	(64, 28, 28, 10)	110,656
	GroupNorm	(64, 28, 28, 10)	128
Residual block	Conv3d	(64, 28, 28, 10)	110,656
	GroupNorm	(64, 28, 28, 10)	128
	LeakyReLU	(64, 28, 28, 10)	0
	Conv3d	(64, 28, 28, 10)	110,656
	GroupNorm	(64, 28, 28, 10)	128
Residual block	Conv3d	(64, 28, 28, 10)	110,656
	GroupNorm	(64, 28, 28, 10)	128
	LeakyReLU	(64, 28, 28, 10)	0
	Conv3d	(64, 28, 28, 10)	110,656
	GroupNorm	(64, 10, 28, 10)	128

Deconvolutional Layers

Block type	Layer type	Output shape	# of parameters
Deconvolution block	Upsample	(128, 28 28, 10)	0
	Conv3d	(64, 28 28, 10)	221,248
	GroupNorm	(64, 28 28, 10)	128
	LeakyReLU	(64, 28 28, 10)	0
Deconvolution block	Upsample	(128, 56 56, 20)	0
	Conv3d	(32, 56 56, 20)	110,624
	GroupNorm	(32, 56 56, 20)	64
	LeakyReLU	(32, 56 56, 20)	0
Deconvolution block	Upsample	(64, 56 56, 20)	0
	Conv3d	(32, 56 56, 20)	55,328
	GroupNorm	(32, 56 56, 20)	64
	LeakyReLU	(32, 56 56, 20)	0
Deconvolution block	Upsample	(32, 56 56, 20)	0
	Conv3d	(16, 56 56, 20)	27,664
	GroupNorm	(16, 56 56, 20)	32
	LeakyReLU	(16, 56 56, 20)	0
	Conv3d	(1,56 56, 20)	433
	GELU	(1,56 56, 20)	0
	Decoder	(1,56 56, 20)	0
			1,510,673

Figure 2. A breakdown of the U-Net model's layer specifications including output shapes and the parameter counts for each layer. The output shape is represented in four dimensions, capturing the number of filter layers and input dimensions along the x-, y-, and z-directions, respectively. The kernel size is 3 × 3 and the paddings are not shown in the table.

We train three different surrogate models using the same proposed U-Net architecture, each with one type of output data: pressure, vertical displacement, or CO_2 plume/saturation. Each model maps from well location information combined with permeability field directly to the 3-D state variables of interest. The mapping process of the U-Net model can be formulated as

$$\hat{Y} = F_{unet1}(x, m), \hat{Y} \in \mathbb{R}^{H \times W \times D}, x \in \mathbb{R}^{H \times W \times D}, m \in \mathbb{R}^{H \times W \times D} \tag{1}$$

where $\hat{Y}$ represents the model output which has three-dimension: H, W, D that represent the first, second, and third coordinate direction of the output field, respectively. F_{unet1} represents the mapping process of the U-Net model. The input, x, represents the well location field in 3-D with dimensions of H, W, D that represent the first, second, and third coordinate direction, respectively. Input m represents the flow property or permeability field in 3-D with dimensions of H, W, D that represent the first, second, and third coordinate direction, respectively. The loss function of the training is defined using MSE loss as

$$\mathcal{L}(Y, \hat{Y}) = \frac{1}{n} \sum_{i=1}^{n} (Y_i - \hat{Y}_i)^2 \tag{2}$$

where n is the total number of sample size, $\hat{Y}$ is the predicted U-Net model output field, and Y is the observed values. The training hyperparameter settings are listed in Table 1.

Training-testing split ratio	0.8
Learning rate	1E-4
Step size	500
Batch size	8
Epochs	1000
Optimizer	Adam (Kingma and Ba, 2014)

Table 1. Training hyperparameter settings.

For predicting the 3-D plastic strain field, a direct mapping from well locations with permeability values to the plastic strain field proves to be ineffective due to the highly localized and sparse nature of the output. We will elaborate on this challenge in the subsequent results section. To overcome this limitation, we have devised a workflow, illustrated in Figure 3, that involves a two-step process. In the first step, we employ a U-Net model to learn the mapping from well locations to pressure, while the second step involves training another U-Net model to map the derived pressure field to the plastic strain field. It's worth noting that both U-Net models share the same structural architecture, differing only in their respective inputs, outputs, and weights of the U-Net models.

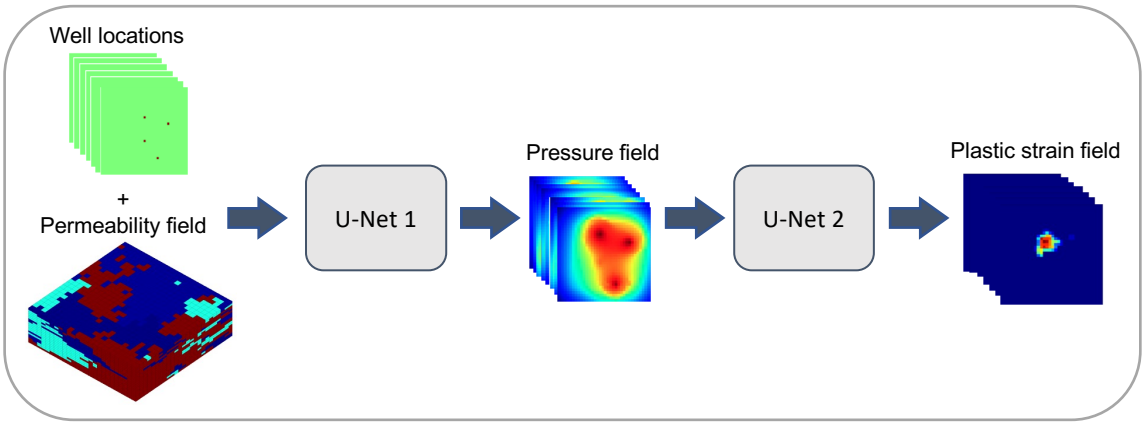

Figure 3. Schematic workflow to map from well location into plastic strain field through two U-Net models.

General Workflow

In this section, we describe a schematic workflow as depicted in Figure 4 for the construction of U-Net models aimed at predicting various simulation results, including pressure, CO_2 saturation, vertical displacement, and effective plastic strain, from well location information and permeability field data. We start with data preparation step where we establish a coupled-physics reservoir simulation model to facilitate data generation. Subsequently, we generate a comprehensive training dataset by executing reservoir simulations under a variety of well configurations, resulting in 3-D outputs of pressure, CO_2 saturation, vertical displacement, and effective plastic strain. The detailed data generation process is elaborated in Appendix A. Following data generation, we perform min-max normalization on each of the diverse inputs and outputs to prepare them for training.

In the training step, we first construct and train the fundamental U-Net architecture as illustrated on Figure 1 to establish the mapping from well location information with permeability field to the final time step simulation results of pressure, CO_2 saturation, and vertical displacement. We then perform fine-tuning of the model structure and adjusting training hyperparameters to optimize the model's performance. Subsequently, we undertake a sensitivity analysis to determine the minimum required sample size for effective training. Moving on to the training step 2, in this step, we build and train the same U-Net structure with input as the predicted pressure from U-Net 1 and output as the effective plastic strain field. The fine tuning and sensitivity analysis on training sample size is also performed for this model and summarized in Appendix B.

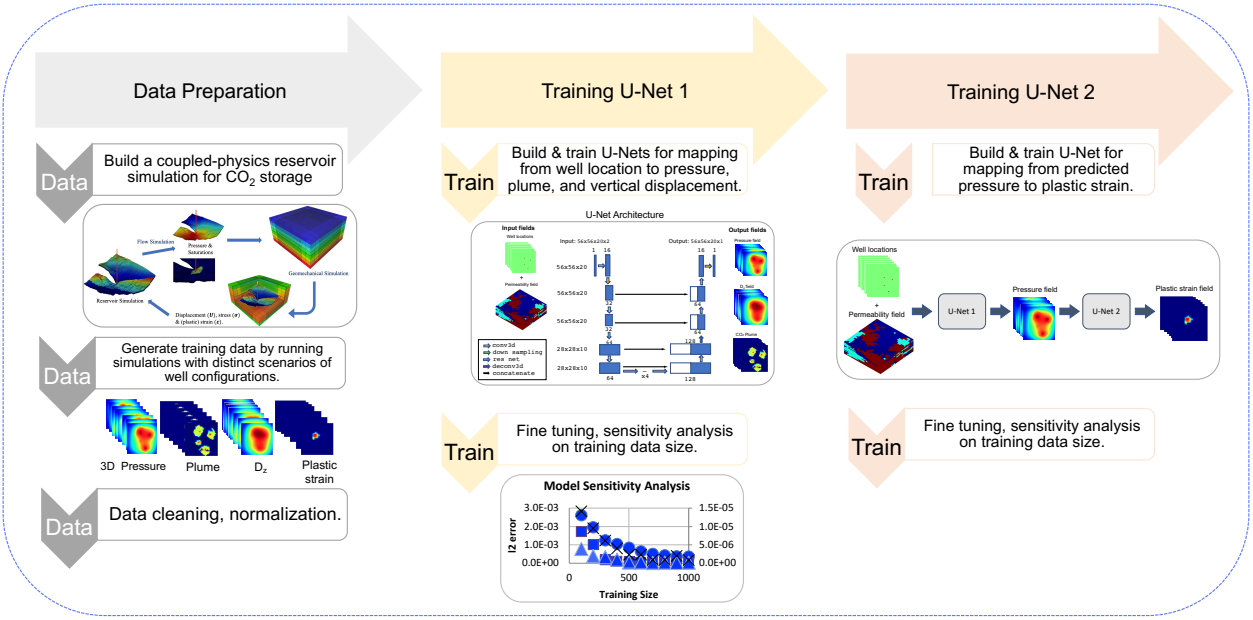

Figure 4. General workflow for building and training U-Net models.

Results and Discussion

U-Net with permeability

In this section, we present the results and show the performance of the proposed U-Net model with permeability concatenated with well location information as the input data. A total of 200 unseen testing data is used to test the performance of the four U-Net models. The testing MSEs are summarized in Table B1. Figure 5 shows the plots of the results for pressure prediction using the U-Net model for 11 selected cases. In the first row, the maps display the locations of wells denoted by green and black dots on the permeability map for each of the 11 cases at the injection layer (17^{th} layer). In the second row, we present the pressure predictions at the injection layer. The first plot within the dashed box identifies the region of heterogeneous permeability. The third row illustrates the actual pressure observations at the same layer. Lastly, the fourth row depicts the mismatch between the predicted pressure and the true pressure observations. In the fourth row, it is evident that the proposed U-Net model demonstrates superior predictions, exhibiting minimal spatial mismatch values. A similar trend emerges when applying the proposed U-Net model to vertical displacement, as depicted in Figure 6 for vertical displacement prediction. It's worth noting that the mismatch in the case of vertical displacement is notably smaller than that observed for pressure, primarily due to the smoother nature of the vertical displacement field. Figure 7 provides a visual representation of the prediction results for CO_2 saturation. The comparison between predicted and observed values reveals a good match, although a relatively higher mismatch is noticeable, particularly in the boundary cells of the CO_2 plume. This discrepancy can be attributed to the inherently less smooth (Rahaman et al., 2019; Cao et al., 2019) and sparser nature of the CO_2 saturation field. The vertical (x-z) views of the CO_2 saturation prediction results are shown on Figure 8. In both figures, a strong alignment is evident between the predicted and actual CO_2 saturation field, highlighting the U-Net's capability to capture both horizontal and vertical spatial correlations.

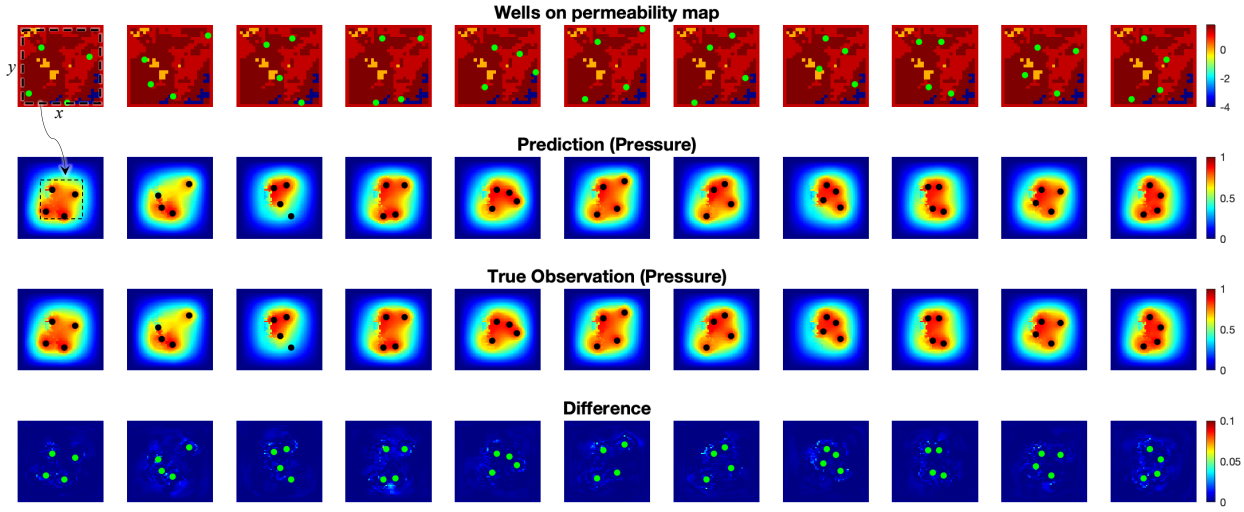

Figure 5. U-Net model prediction for pressure (with permeability as one of the input data). The green and black dots are well locations shown on the map. The first row plots the wells on permeability map for each of the 11 cases. The second row shows the pressure prediction at the injection layer. The heterogeneous permeability region is labelled at the first plot inside the dashed box. The third row shows the true observation of pressure at the same layer, and the fourth row shows the difference between predicted pressure and the true observation of pressure.

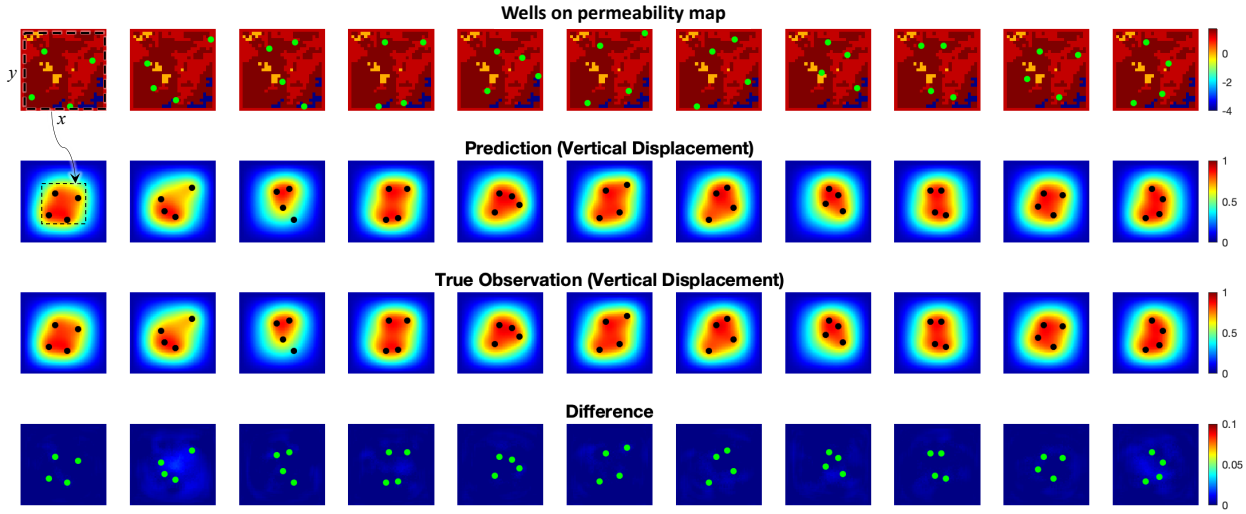

Figure 6. U-Net model prediction for vertical displacement, D_z (with permeability as one of the input data). The green and black dots are well locations shown on the map. The first row plots the wells on permeability map for each of the 11 cases. The second row shows the D_z prediction at the injection layer. The heterogeneous permeability region is labelled at the first plot inside the dashed box. The third row shows the true observation of D_z at the same layer, and the fourth row shows the difference between predicted D_z and the true observation of D_z.

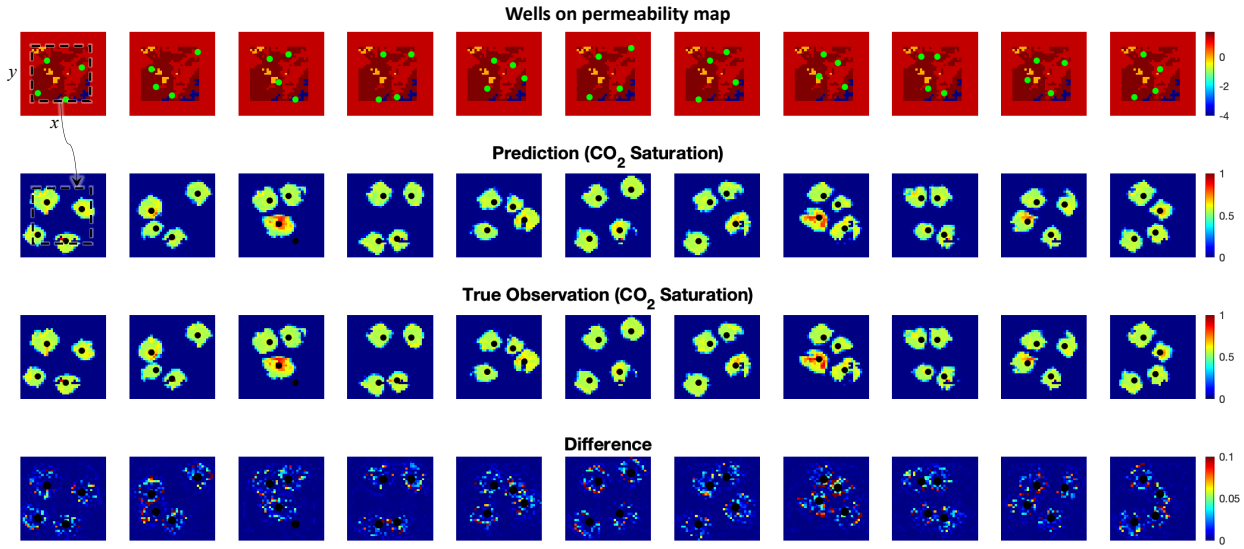

Figure 7. U-Net model prediction for CO_2 Saturation (with permeability as one of the input data). The green and black dots are well locations shown on the map. The first row plots the wells on permeability map for each of the 11 cases. The second row shows the CO_2 Saturation prediction at the injection layer. The heterogeneous permeability region is labelled at the first plot inside the dashed box. The third row shows the true observation of CO_2 Saturation at the same layer, and the fourth row shows the difference between predicted and the true observation of CO_2 Saturation.

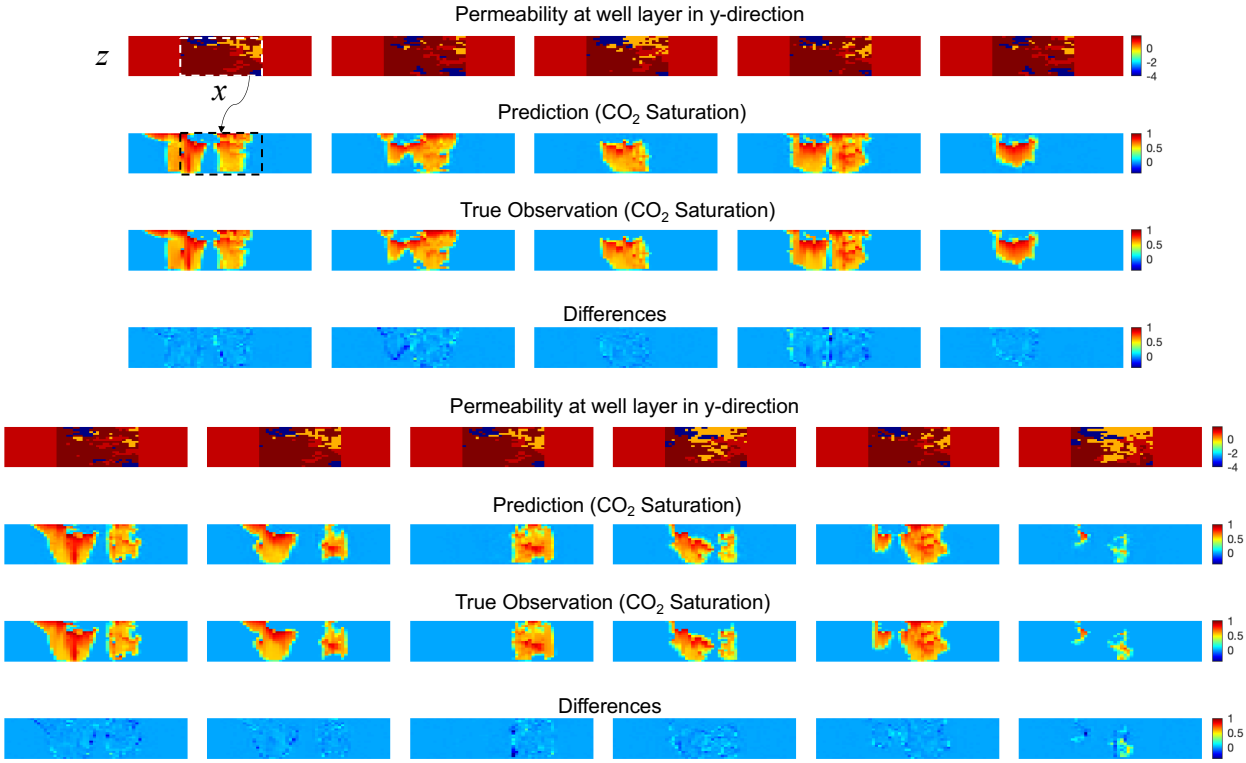

Figure 8. U-Net model prediction for CO_2 Saturation (vertical view) with permeability as one of the input data for the corresponding 11 examples in Figure 7.

We perform multiple scenarios for the training of effective plastic strain with different input structure and loss functions. The testing MSE errors are summarized in Table 2. Figure 9 provides a visual representation of the prediction results for effective plastic strain across multiple training scenarios in

Table 2. Both the table and the plots clearly indicate that the testing error is minimized when using predicted pressure (case 4) as the training input for the same training hyperparameter settings. We also observe that when Mean Squared Error (MSE) is used as the loss function, the sparsity of the output data can lead to a very small MSE value during the initial training iterations, causing the training to converge too rapidly without sufficiently capturing the input-output relationship.

Additionally, it is worth noting that incorporating the permeability map alongside well location data as input results in deteriorated training performance. This phenomenon can be attributed to the fact that the output variable, effective plastic strain, exhibits strong localization around the well locations. When permeability information is introduced as part of the input, it tends to overshadow the significance of well locations. This observation becomes evident when analyzing the feature maps of the convolutional layers, as depicted in Figure 10. In Figure 10, we focus on the feature maps within convolutional block no. 3, using a model input comprising well location information concatenated with permeability maps. The first row displays the 16 feature map layers for well configuration 1, with the well locations depicted in the final column. The second row illustrates the difference between feature maps at the same locations between well configuration 1 and 0 (not shown here). The third row showcases the feature maps at the same locations for well configuration 2, and the fourth row illustrates the difference between feature maps at the same locations between well configuration 1 and 2.

From the plots, it becomes evident that the inclusion of permeability data in the input leads to a near disappearance of the well location information in the feature maps, which is only discernible when subtracting the permeability information. In contrast, the feature maps that have undergone permeability subtraction, as shown in the second and fourth rows, successfully preserve the original well locations and exhibit noticeable distinctions among different well configurations. However, when permeability information remains uncompensated, as depicted in the first and third rows, the localized well information becomes indistinguishable, and the feature maps display minimal differences among various well configurations. Furthermore, an analysis of the colorbar reveals that the well location information represents only 0.2% of the permeability information. This underscores the ease with which well location information can be overshadowed when combined with permeability data. Considering the localized and sparse nature of the effective plastic strain output variable, it is imperative to emphasize local information in the input to enable the model to effectively capture the input-output relationship during training. With these observations and conclusion, we conducted another study in which we assign greater importance to the well location input. Table 2 case 2 displays the testing mean squared error (MSE), and it clearly demonstrates that increasing the weight on well location information leads to improved training performance than that of case 1 and case 3. The weight factor must be determined through a sensitivity analysis.

Case	Input 1	Weight for input 1	Input 2	Weight for input 2	Testing MSE Error
1	**well location**	1	permeability map	1	1.51E-05
2	**well location**	1E4	permeability map	1	1.709E-06
3	**well location**	1	-	-	9.384E-06
4	**predicted pressure**	1	-	-	8.810E-07

Table 2. Testing errors across various training scenarios for effective plastic strain with the same hyperparameter settings.

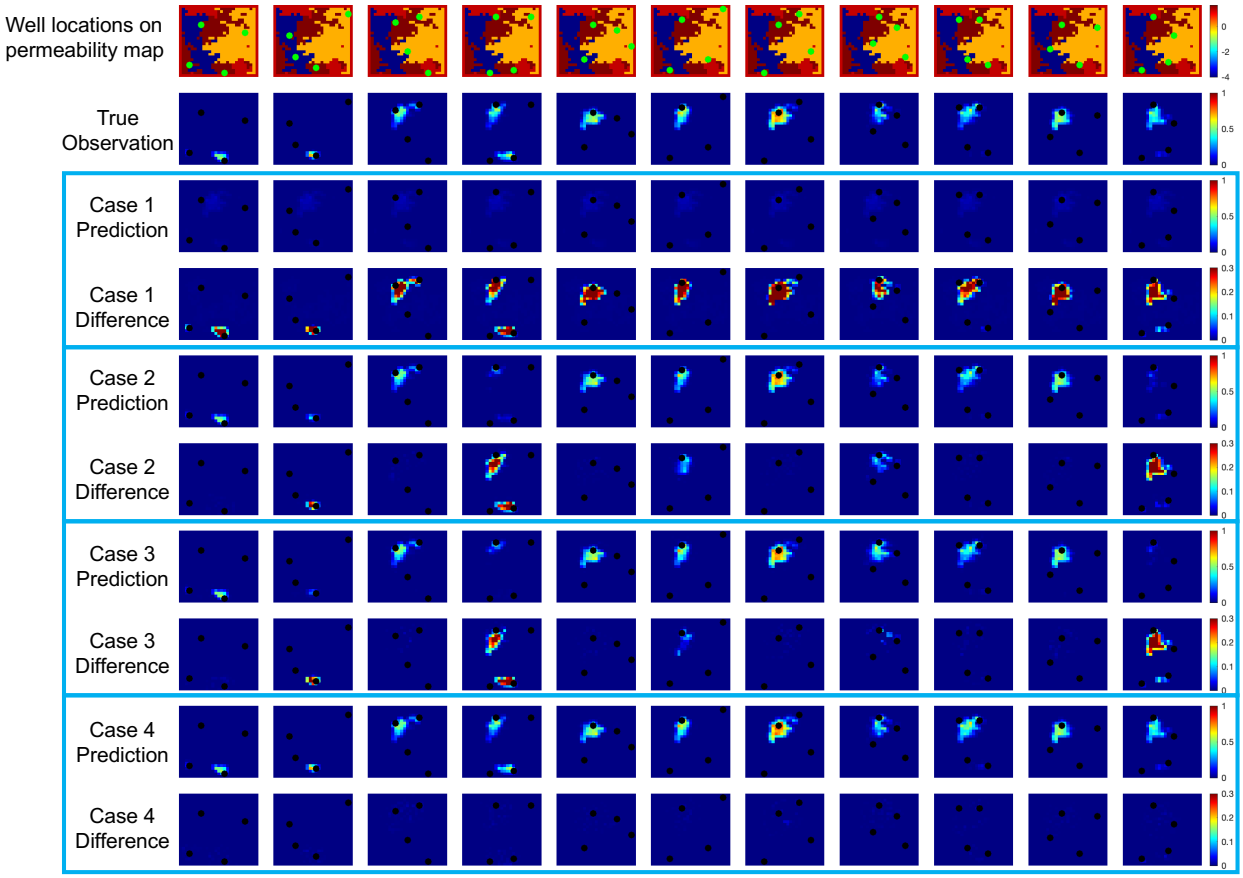

Figure 9. Different cases on Table 2 of U-Net model prediction for effective plastic strain (ε_p'). The green and black dots are well locations shown on the map. The first row shows the well locations on permeability maps. The second row plots the true observation for each of the 11 cases. The rest of the rows show the prediction and mismatch at the first layer for each case.

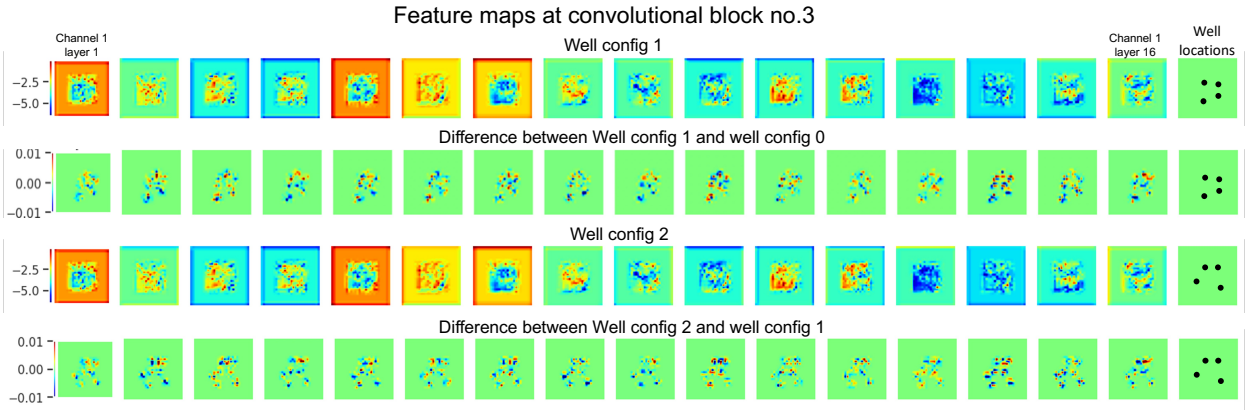

Figure 10. Feature maps at convolutional block no.3 with model input of well location information concatenated with permeability maps. The first row plots the 16 layers on channel 1 for well configuration 1 with well locations plotted on the last column. The second row shows the difference between the feature maps at the same location between well configuration 1 and 0 (which is not shown here). The third row shows the feature maps at the same location for well configuration 2 and the fourth row shows the difference between the feature maps at the same location between well configuration 1 and 2.

U-Net without permeability

When training the model for prediction of non-sparse and smoother parameters, such as pressure, vertical displacement, and CO_2 saturation, the absence of permeability results in degraded training performance

compared to when permeability is included, under the same model training settings. As demonstrated by the discrepancies in vertical displacement and CO_2 saturation predictions, some testing cases exhibit significant underestimation, indicating a substantial gap between predicted values and true observations. This underscores the importance of incorporating the permeability field into the model input, as it enables the model to learn more quickly about the input-output relationship with a better representation of global spatial information.

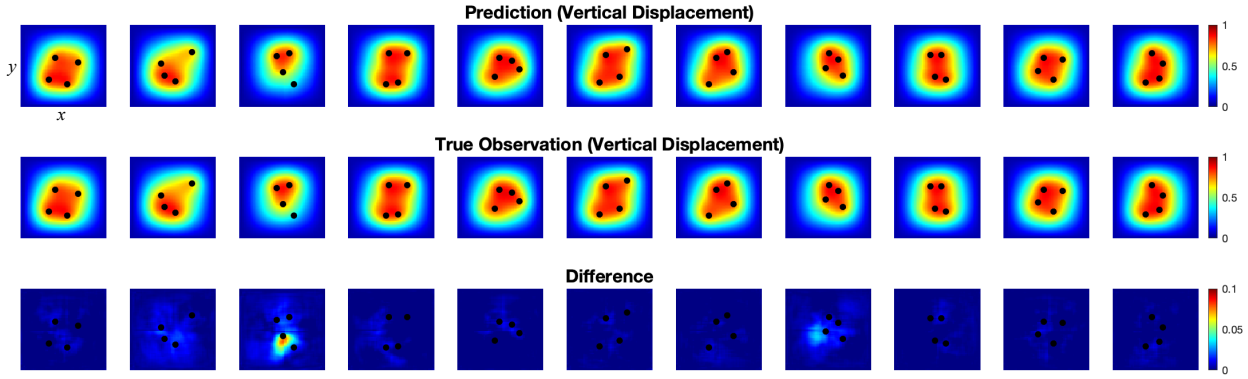

Figure 11. U-Net model prediction for vertical displacement, D_z (without permeability for the input data). The green and black dots are well locations shown on the map. The first row plots the wells on permeability map for each of the 11 cases. The second row shows the D_z prediction at the injection layer. The heterogeneous permeability region is labelled at the first plot inside the dashed box. The third row shows the true observation of D_z at the same layer, and the fourth row shows the difference between predicted D_z and the true observation of D_z.

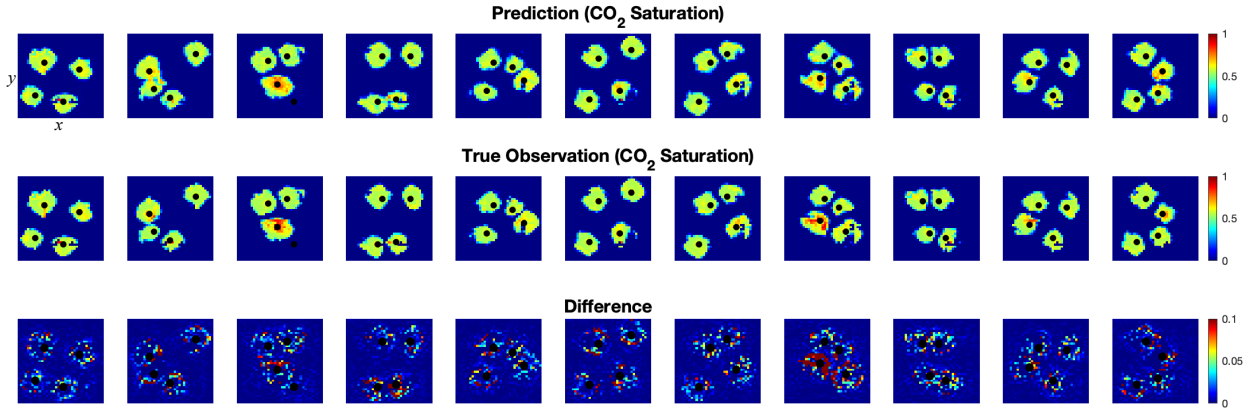

Figure 12. U-Net model prediction for CO_2 Saturation (without permeability for the input data). The green and black dots are well locations shown on the map. The first row plots the wells on permeability map for each of the 11 cases. The second row shows the CO_2 Saturation prediction at the injection layer. The heterogeneous permeability region is labelled at the first plot inside the dashed box. The third row shows the true observation of CO_2 Saturation at the same layer, and the fourth row shows the difference between predicted and the true observation of CO_2 Saturation.

Conclusions

In this paper, we proposed a U-Net model to approximate the output of a coupled flow and geomechanics model for different well configurations. The model uses the permeability model concatenated with well location information as input to predict the spatiotemporal distribution of pressure, flow, and important geomechanical output. We evaluated the performance of the model on 200 instances of unseen test data for prediction of multiple parameters, including pressure, vertical displacement, CO_2 saturation, and effective plastic strain. For pressure, vertical displacement, and CO_2 saturation predictions, the inclusion of permeability data in the input significantly improved the model training and prediction performance. The training results demonstrated that the proposed U-Net model produced predictions that closely matched the true responses, especially those that have global nature such as pressure. In predicting CO_2 saturation, while there was generally a good match between predicted and observed values, some

discrepancies were observed, particularly in boundary cells. This discrepancy could be attributed to the inherent non-smooth nature of the CO_2 saturation field. Nonetheless, the proposed U-Net model was able to capture both horizontal and vertical distribution of the saturation distribution. We also explored different training scenarios for predicting the effective plastic strain, considering various input structures and loss functions. We observed that only including the permeability map alongside well location data as input could lead to deteriorated training performance for effective plastic strain prediction. However, including pressure information as input improved the prediction error of the effective plastic strain. In summary, our study demonstrated the effectiveness of the proposed U-Net model in predicting various subsurface parameters, with the inclusion of permeability data enhancing performance for non-sparse parameters. The choice of training inputs and the balance between well location and permeability information were found to be crucial in achieving accurate predictions, emphasizing the need for thoughtful model configuration and sensitivity analysis in subsurface modeling applications.

References

Agada, S., Geiger, S., Elsheikh, A. and Oladyshkin, S., 2017. Data-driven surrogates for rapid simulation and optimization of WAG injection in fractured carbonate reservoirs. Petroleum Geoscience, 23(2), pp.270-283.

Al-Mudhafar, W.J. and Rao, D.N., 2017, April. Proxy-based metamodeling optimization of the gas-assisted gravity drainage GAGD process in heterogeneous sandstone reservoirs. In SPE Western Regional Meeting. OnePetro.

Al-Mudhafar, W.J., Rao, D.N., Srinivasan, S., Vo Thanh, H. and Al Lawe, E.M., 2022. Rapid evaluation and optimization of carbon dioxide-enhanced oil recovery using reduced-physics proxy models. Energy Science & Engineering, 10(10), pp.4112-4135.

Alenezi, F. and Mohaghegh, S., 2016, November. A data-driven smart proxy model for a comprehensive reservoir simulation. In 2016 4th Saudi International Conference on Information Technology (Big Data Analysis)(KACSTIT) (pp. 1-6). IEEE.

Bahrami, P., Sahari Moghaddam, F. and James, L.A., 2022. A Review of Proxy Modeling Highlighting Applications for Reservoir Engineering. Energies, 15(14), p.5247.

Burton M, Kumar N, Bryant SL. Time-dependent injectivity during CO2 storage in aquifers. Paper SPE 113937; SPE/DOE Improved Oil Recovery Symposium, Tulsa, Oklahoma; 19–23 April 2008.

Cao, Y., Fang, Z., Wu, Y., Zhou, D.X. and Gu, Q., 2019. Towards understanding the spectral bias of deep learning. arXiv preprint arXiv:1912.01198.

Cardoso, M.A., Durlofsky, L.J. and Sarma, P., 2009. Development and application of reduced-order modeling procedures for subsurface flow simulation. International journal for numerical methods in engineering, 77(9), pp.1322-1350.

Chen, B., Harp, D.R., Lin, Y., Keating, E.H. and Pawar, R.J., 2018. Geologic CO2 sequestration monitoring design: A machine learning and uncertainty quantification based approach. Applied energy, 225, pp.332-345.

Chen, S., Zhao, S. and Lan, Q., 2022. Residual block based nested U-type architecture for multi-modal brain tumor image segmentation. Frontiers in Neuroscience, 16, p.832824.

Chu, C. (1990). Prediction of steamflood performance in heavy oil reservoirs using correlations developed by factorial design method. Paper presented at the SPE California Regional Meeting.

Dejean, J., & Blanc, G. (1999). Managing uncertainties on production predictions using integrated statistical methods. Paper presented at the SPE Annual Technical Conference and Exhibition.

Eide, A.L., Holden, L., Reiso, E. and Aanonsen, S.I., 1994, June. Automatic history matching by use of response surfaces and experimental design. In ECMOR IV-4th European conference on the mathematics of oil recovery (pp. cp-233). European Association of Geoscientists & Engineers.

Elvind D, Asmund H, Rolf V (1992) Maximum information at minimum cost: a North Sea field development study with an experimental design. J Petrol Technol 44(12):1,350–351,356

Friedmann, F., Chawathe, A. and Larue, D.K., 2003. Assessing uncertainty in channelized reservoirs using experimental designs. SPE Reservoir Evaluation & Engineering, 6(04), pp.264-274.

Ganesh, P.R. and Mishra, S., 2014. Reduced physics modeling of CO2 injectivity. Energy Procedia, 63, pp.3116-3125.

Gasda SE, Nordbotten JM, Celia MA. Application of simplified models to CO2 migration and immobilization in large-scale geological systems. Intl Journal of Greenhouse Gas Control 2012; Vol. 9, p. 72–84.

Ghasemi, M., Yang, Y., Gildin, E., Efendiev, Y. and Calo, V., 2015, February. Fast multiscale reservoir simulations using pod-deim model reduction. In SPE reservoir simulation symposium. OnePetro.

Gilmore, K.A., Sahu, C.K., Benham, G.P., Neufeld, J.A. and Bickle, M.J., 2022. Leakage dynamics of fault zones: Experimental and analytical study with application to CO2 storage. Journal of Fluid Mechanics, 931, p.A31.

Güyagüler, B. and Horne, R.N., 2004. Uncertainty assessment of well-placement optimization. SPE Reservoir Evaluation & Engineering, 7(01), pp.24-32.

Harp, D.R., Pawar, R., Carey, J.W. and Gable, C.W., 2016. Reduced order models of transient CO2 and brine leakage along abandoned wellbores from geologic carbon sequestration reservoirs. *International Journal of Greenhouse Gas Control*, *45*, pp.150-162.

He, J. and Durlofsky, L.J., 2014. Reduced-order modeling for compositional simulation by use of trajectory piecewise linearization. SPE Journal, 19(05), pp.858-872.

Hendrycks, D. and Gimpel, K., 2016. Gaussian error linear units (gelus). arXiv preprint arXiv:1606.08415.

Jaber, A.K., Al-Jawad, S.N. and Alhuraishawy, A.K., 2019. A review of proxy modeling applications in numerical reservoir simulation. Arabian Journal of Geosciences, 12(22), p.701.

Jia, W., McPherson, B.J., Pan, F., Xiao, T. and Bromhal, G., 2016. Probabilistic analysis of CO2 storage mechanisms in a CO2-EOR field using polynomial chaos expansion. *International Journal of Greenhouse Gas Control*, *51*, pp.218-229.

Jiang, Z., Tahmasebi, P. and Mao, Z., 2021. Deep residual U-net convolution neural networks with autoregressive strategy for fluid flow predictions in large-scale geosystems. Advances in Water Resources, 150, p.103878.

Jiang, Z., Zhu, M., Li, D., Li, Q., Yuan, Y.O. and Lu, L., 2023. Fourier-MIONet: Fourier-enhanced multiple-input neural operators for multiphase modeling of geological carbon sequestration. arXiv preprint arXiv:2303.04778.

Jin, Z.L. and Durlofsky, L.J., 2018. Reduced-order modeling of CO2 storage operations. *International Journal of Greenhouse Gas Control*, *68*, pp.49-67.

Kabir, C.S., Chawathe, A., Jenkins, S.D., Olayomi, A.J., Aigbe, C. and Faparusi, D.B., 2004. Developing new fields using probabilistic reservoir forecasting. SPE Reservoir Evaluation & Engineering, 7(01), pp.15-23.

Kalla, S. and White, C.D., 2007. Efficient design of reservoir simulation studies for development and optimization. SPE Reservoir Evaluation & Engineering, 10(06), pp.629-637.

Keating, E., Bacon, D., Carroll, S., Mansoor, K., Sun, Y., Zheng, L., Harp, D. and Dai, Z., 2016. Applicability of aquifer impact models to support decisions at CO2 sequestration sites. *International Journal of Greenhouse Gas Control*, *52*, pp.319-330.

Khanal, A. and Shahriar, M.F., 2022. Physics-based proxy modeling of CO2 sequestration in deep saline aquifers. Energies, 15(12), p.4350.

Kingma, D.P. and Ba, J., 2014. Adam: A method for stochastic optimization. arXiv preprint arXiv:1412.6980.

Landa, J.L. and Guyaguler, B., 2003, October. A methodology for history matching and the assessment of uncertainties associated with flow prediction. In SPE Annual Technical Conference and Exhibition. OnePetro.

Latrach, A., Malki, M.L., Morales, M., Mehana, M. and Rabiei, M., 2023. A Critical Review of Physics-Informed Machine Learning Applications in Subsurface Energy Systems. arXiv preprint arXiv:2308.04457.

Li, B. and Friedmann, F., 2005, January. Novel multiple resolutions design of experiment/response surface methodology for uncertainty analysis of reservoir simulation forecasts. In SPE Reservoir Simulation Symposium. OnePetro.

Liu, M., Vashisth, D., Grana, D. and Mukerji, T., 2023. Joint Inversion of Geophysical Data for Geologic Carbon Sequestration Monitoring: A Differentiable Physics-Informed Neural Network Model. Journal of Geophysical Research: Solid Earth, 128(3), p.e2022JB025372.

Manceau, E., Mezghani, M., Zabalza-Mezghani, I. and Roggero, F., 2001, September. Combination of experimental design and joint modeling methods for quantifying the risk associated with deterministic and stochastic uncertainties-an integrated test study. In SPE Annual Technical Conference and Exhibition. OnePetro.

Meguerdijian, S., Pawar, R.J., Chen, B., Gable, C.W., Miller, T.A. and Jha, B., 2023. Physics-informed machine learning for fault-leakage reduced-order modeling. International Journal of Greenhouse Gas Control, 125, p.103873.

Nair, V. and Hinton, G.E., 2010. Rectified linear units improve restricted boltzmann machines. In Proceedings of the 27th international conference on machine learning (ICML-10) (pp. 807-814).

Noh M, Lake LW, Bryant SL, Araque-Martinez A. Implications of coupling fractional flow and geochemistry for CO2 injection in aquifers.SPE Reservoir Engineering and Evaluation 2007; Vol. 10(4), p. 406–411.

Oruganti Y, and Mishra S. An improved simplified analytical model for CO2 plume movement and pressure buildup in deep saline formations. International Journal of Greenhouse Gas Control 2013; Vol. 14, p. 49-59; DOI: 10.1016/j.ijggc.2012.12.024.

Pan, I., Babaei, M., Korre, A. and Durucan, S., 2014. Artificial Neural Network based surrogate modelling for multi-objective optimisation of geological CO2 storage operations. Energy Procedia, 63, pp.3483-3491.

Qin, Z., Jiang, A., Faulder, D., Cladouhos, T.T. and Jafarpour, B., 2023. Efficient Optimization of Energy Recovery From Geothermal Reservoirs With Recurrent Neural Network Predictive Models. Water Resources Research, 59(3), p.e2022WR032653.

Rahaman, N., Baratin, A., Arpit, D., Draxler, F., Lin, M., Hamprecht, F., Bengio, Y. and Courville, A., 2019, May. On the spectral bias of neural networks. In International Conference on Machine Learning (pp. 5301-5310). PMLR.

Saripalli, P. and McGrail, P., 2002. Semi-analytical approaches to modeling deep well injection of CO2 for geological sequestration. Energy Conversion and Management, 43(2), pp.185-198.

Sayyafzadeh, M., 2017. Reducing the computation time of well placement optimisation problems using self-adaptive metamodelling. Journal of Petroleum Science and Engineering, 151, pp.143-158.

Schuetter, J., Ganesh, P.R. and Mooney, D., 2014. Building statistical proxy models for CO2 geologic sequestration. Energy Procedia, 63, pp.3702-3714.

Shokouhi, P., Kumar, V., Prathipati, S., Hosseini, S.A., Giles, C.L. and Kifer, D., 2021. Physics-informed deep learning for prediction of CO2 storage site response. Journal of Contaminant Hydrology, 241, p.103835.

Slotte, P.A. and Smorgrav, E., 2008, June. Response surface methodology approach for history matching and uncertainty assessment of reservoir simulation models. In Europec/EAGE Conference and Exhibition. OnePetro.

Syed, F.I., AlShamsi, A., Dahaghi, A.K. and Neghabhan, S., 2022. Application of ML & AI to model petrophysical and geomechanical properties of shale reservoirs–A systematic literature review. *Petroleum*, *8*(2), pp.158-166.

Tang, M., Ju, X. and Durlofsky, L.J., 2022. Deep-learning-based coupled flow-geomechanics surrogate model for CO2 sequestration. International Journal of Greenhouse Gas Control, 118, p.103692.

Tariq, Z., Yan, B. and Sun, S., 2023, January. Physics Informed Surrogate Model Development in Predicting Dynamic Temporal and Spatial Variations During CO2 Injection into Deep Saline Aquifers. In SPE Reservoir Characterisation and Simulation Conference and Exhibition? (p. D021S010R002). SPE.

Van Doren, J.F., Markovinović, R. and Jansen, J.D., 2006. Reduced-order optimal control of water flooding using proper orthogonal decomposition. Computational Geosciences, 10, pp.137-158.

Wen, G., Li, Z., Azizzadenesheli, K., Anandkumar, A. and Benson, S.M., 2022. U-FNO—An enhanced Fourier neural operator-based deep-learning model for multiphase flow. Advances in Water Resources, 163, p.104180.

White, C.D. and Royer, S.A., 2003, February. Experimental design as a framework for reservoir studies. In SPE Reservoir Simulation Symposium. OnePetro.

Yan, B., Harp, D.R., Chen, B. and Pawar, R., 2022. A physics-constrained deep learning model for simulating multiphase flow in 3D heterogeneous porous media. Fuel, 313, p.122693.

Yeten, B., Castellini, A., Guyaguler, B. and Chen, W.H., 2005, January. A comparison study on experimental design and response surface methodologies. In SPE Reservoir Simulation Symposium. OnePetro.

Zheng, F., Jahandideh, A., Jha, B. and Jafarpour, B., 2021. Geologic CO2 storage optimization under geomechanical risk using coupled-physics models. International Journal of Greenhouse Gas Control, 110, p.103385.

Zheng, F., Jha, B. and Jafarpour, B., 2023, October. Controlled CO2 Injection into Storage Reservoirs to Minimize Geomechanical Risks Under Geologic Uncertainty. In SPE Annual Technical Conference and Exhibition? (p. D021S020R005). SPE.

Zhong, Z., Sun, A.Y. and Jeong, H., 2019. Predicting CO2 plume migration in heterogeneous formations using conditional deep convolutional generative adversarial network. Water Resources Research, 55(7), pp.5830-5851.

Appendix A. Training Dataset Generation

In this section, we describe the process to generate training dataset for the surrogate model. The numerical simulation model described in our previous paper (Zheng et al., 2021) Numerical Experiment Results Section, Example 2: Multi-facies Model is used for the data generation. A total of 1000 reservoir simulations are executed, each featuring distinct well locations under a consistent Bottom Hole Pressure (BHP) control setting. Each simulation run is configured with four wells. To encompass a broad spectrum of well configurations, we partition the heterogeneous region into four quadrants, as illustrated in Figure A1. Each well is then randomly assigned to one of these quadrants. Furthermore, we maintain a minimum inter-well distance of 500 meters, which spans over three grid blocks to ensure an appropriate separation between the wells.

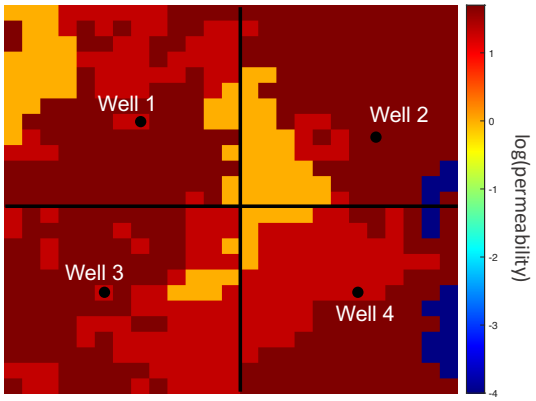

Figure A1. Four quadrants on the heterogeneous permeability region.

Appendix B. Sensitivity Analysis of Surrogate Model

In this section, we present a sensitivity analysis of the proposed surrogate model concerning the determination of training data size. The training is conducted using the U-Net models outlined in Section 2.1 to predict the final-time step values for pressure, CO_2 plume, vertical displacement (D_z), and effective plastic strain (ε_p'). We explore the impact of varying training data sizes, ranging from 100 to 1000 data points, while maintaining a consistent 4:1 ratio between training and testing datasets. For testing purposes, we employ a fixed set of 200 additional, previously unseen data points for each training scenario. Table B1 provides a comprehensive summary of the Mean Squared Error (MSE) for different prediction parameters, encompassing pressure, CO_2 plume saturation, vertical displacement, and effective plastic strain. We also investigate the influence of including or excluding permeability information. Concurrently, Figure B1 depicts a graphical representation of the MSE error in relation to the training data size for all four parameters. Upon examining the results presented in Table B1 and Figure B1, it becomes evident that there is a consistent trend of decreasing MSE error as the training data size increases for all four parameters. Specifically, a convergence in the MSE error is observed for pressure and vertical displacement when the training size reaches 500, suggesting that little additional improvement in training performance is achieved beyond this point. Therefore, a training size of 500 data points is deemed sufficient to yield highly accurate testing results for predicting pressure and vertical displacement. Similarly, the convergence for CO_2 saturation and effective plastic strain is observed at a training size of 700, indicating that there is minimal room for improvement in training performance beyond this threshold. Consequently, we establish a minimum data size requirement of 700 data points for training models aimed at predicting CO_2 saturation and effective plastic strain. Additionally, the availability of permeability information played a crucial role in enhancing prediction accuracy. When permeability information was not included, the predictive performance for pressure, vertical displacement, and CO_2 saturation experienced a decline.

Prediction Parameter	*Data Size*	*Testing Error (MSE)*	*Permeability Information (y/n)*	*Prediction Parameter*	*Data Size*	*Testing Error (MSE)*	*Permeability Information (y/n)*
Pressure	100	7.822E-04	y	***Vertical Displacement***	100	1.720E-03	y
	200	3.843E-04	y		200	1.007E-03	y
	300	3.337E-04	y		300	1.666E-04	y
	400	1.986E-04	y		400	1.100E-04	y
	500	4.454E-05	y		500	6.071E-05	y
	600	4.366E-05	y		600	2.574E-05	y
	700	1.542E-05	y		700	1.101E-05	y
	800	2.056E-05	y		800	8.517E-06	y
	900	2.026E-05	y		900	2.852E-06	y
	1000	1.934E-05	y		1000	6.522E-06	y
	1000	4.861E-04	n		1000	3.724E-05	n
CO_2 Saturation	100	2.617E-03	y	***Effective Plastic Strain***	100	1.416E-05	y
	200	1.961E-03	y		200	9.537E-06	y
	300	1.242E-03	y		300	6.155E-06	y
	400	1.039E-03	y		400	3.985E-06	y
	500	8.470E-04	y		500	2.316E-06	y
	600	6.370E-04	y		600	2.344E-06	y
	700	5.123E-04	y		700	9.507E-07	y
	800	4.312E-04	y		800	9.134E-07	y
	900	3.709E-04	y		900	2.025E-06	y
	1000	3.618E-04	y		1000	8.810E-07	y
	1000	1.218E-03	n				

Table B1. A summary of the Mean Squared Error (MSE) for four U-Net models including mapping to pressure, CO_2 plume/saturation, vertical displacement (D_z), and effective plastic strain (ε_p'), considering different training data sizes and the presence (y) or absence (n) of permeability information.

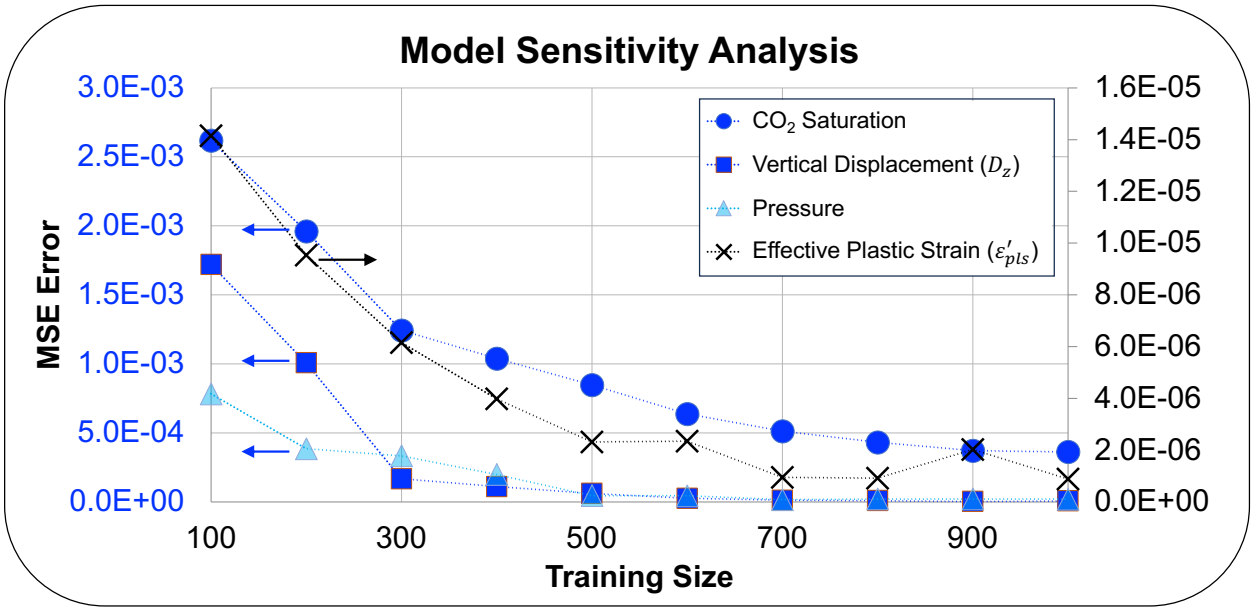

Figure B1. Model sensitivity analysis on training sample size. The y-left axis is the MSE error plotted for CO_2 saturation, vertical displacement (D_z), and pressure while the y-right axis is the MSE error plotted for effective plastic strain.